Astron. Astrophys. 62, 375—392 (1978)

ASTRONOMY AND ASTROPHYSICS

Multifrequency Observations of Very Large Radio Galaxies:

I. 3C 326

A. G. Willis[1]* and R. G. Strom[2]

[1] Sterrewacht Leiden, Huygens Laboratorium, Wassenaarseweg 78, NL-2405 Leiden, The Netherlands
[2] Netherlands Foundation for Radio Astronomy, Radiosterrenwacht, Oude Hoogeveensedijk 4, Dwingeloo, The Netherlands

Received February 22, revised July 11, 1977

Summary. Observations of the radio source 3C 326 at wavelengths of 49, 21 and 6 cm with the Westerbork radio telescope are discussed. The data show conclusively that 3C 326 is a giant radio galaxy having a projected linear extent of 1.7 Mpc ($H_0=75$ km s^{-1} Mpc^{-1}). A compact, flat spectrum nuclear source is associated with the optical galaxy. The outer radio lobes contain no compact hot spots which individually contribute a predominant amount of the source's flux density. 3C 326 has considerable linear polarization, percentage polarizations of up to 50% and 35% being found at 21 and 49 cm, respectively. The spectrum of the integrated radio emission may be represented by a simple power law with a spectral index $\alpha=-0.82$ ($S\propto\nu^{\alpha}$) on the Véron et al. (1974) scale, at least to wavelengths as short as 11 cm.

The main results from an intercomparison of the observations at different wavelengths are the following:

1) the spectral index varies over the outer radio lobes by, at most, 0.3. This fact implies that *in situ* acceleration of relativistic electrons *must* occur in the outer components of 3C 326.

2) Very little depolarization occurs between 21 and 49 cm, indicating that the density of thermal material in the lobes is ~ 2 to $6\,10^{-5}$ cm^{-3}, if equipartition magnetic field strengths are assumed.

3) The magnetic field of 3C 326 has a highly uniform structure over several hundred kpc and is oriented predominantly along the major axis of the source.

4) The density of any intergalactic gas surrounding 3C 326 is, at most, $\sim 3\,10^{-6}$ cm^{-3}.

Key words: radio galaxies — linear polarization — spectral index — radio source morphology

1. Introduction

Observations of radio galaxies having both large intrinsic and angular sizes afford us a unique opportunity to study the double radio source phenomenon in great detail. Intrinsically large sources must have evolved over a very long period of time and consequently one expects the relativistic electrons responsible for the radio emission to have lost energy both through synchrotron radiation losses and inverse Compton scattering on the universal microwave background. The distribution of the radio spectral index over a source thus allows one to place constraints on the rate of decay or of fresh injection of relativistic electrons. Further, using an aperture synthesis radio telescope such as the one at Westerbork, one obtains a very large number of independent picture elements across sources of large angular size and consequently a very detailed map of structure in the outer radio lobes. Perhaps we will then be led to a better understanding of the relationship between the outer lobes of a double radio galaxy and the nuclear region, suspected to be the ultimate source of the energy supply to the outer lobes, which lies within the optical galaxy.

We have therefore used the Westerbork Synthesis Radio Telescope (WSRT) to make multifrequency studies of several very large radio galaxies. In this paper we discuss the observations of 3C 326. Later papers will be concerned with the sources 3C 236 and DA 240 of which 49 cm maps have already been published (Willis et al., 1974).

To our knowledge, the only previous high resolution aperture synthesis observations of 3C 326 are those of Mackay (1969) who used the Cambridge One Mile Telescope at 408 and 1407 MHz. Mackay noted that 3C 326 lies on a ridge of the North Galactic Spur (see e.g. Holden, 1969) and runs parallel to it. Because he found a particularly low brightness temperature for the source, Mackay suggested that "there is a strong possibility that 3C 326 might be a galactic radio source".

Recent single dish observations of the source at frequencies of 1400 and 1420 MHz with $\sim 10'$ resolution have been published by Bridle et al. (1972) and Baker (1974) respectively. Baker pointed out that the source might have an intrinsic size as large as 4.5 Mpc ($H_0=50$ km s^{-1} Mpc^{-1}) if it were an extragalactic source

Send offprint requests to: R. G. Strom
* *Present address:* Department of Physics, Brandeis University, Waltham, Mass. 02154, USA

Table 1. Observing log for 3C 326

Wavelength (cm)	Field	Location (1950.0)		Time (h)	Interferometer spacing (m)			Date
		RA	Dec		Shortest	Increment	Longest	
49.2	3C 326 +3C 326.1	$15^h51^m15^s$	20°13′00″	2×12	54	36	1458	February, March 1975
21.2	3C 326	15 49 36	20 14 24	2×12	54	36	1458	June, August 1975
6.0	3C 326 (west)	15 49 05.8	20 12 00	2×12	54	36	1458	January, 1976
	3C 326 (east)	15 50 14.4	20 15 00	1×12	54	72	1422	January, 1976
	3C 326 (nucleus)[a]	15 49 54.0	20 14 20	2.2	54	72	1422	January, 1975

[a] The nuclear source is also detected in the 3C 326 (east) map

Table 2. Westerbork map parameters for 3C 326

Wavelength (cm)	49.2	21.2	6.0
Half power width of primary beam (arc min)	82	37	11
Half power width of synthesized antenna pattern (arc s, RA × Dec)	55×159	23×67	7×20
Grating ring minor and major axes (arc min, RA × Dec)	46×134	20×58	2.8×8.1 (1×12^h) 5.6×16.2 (2×12^h)
r.m.s. noise (mJy/ synthesized beam area)	~1.5	~1	~1 (1×12^h) ~0.7 (2×12^h)

associated with one of the two 15^m (red) elliptical galaxies that lie within the boundaries of the radio emission. Our new observations at frequencies of 610 (49.2 cm wavelength), 1415 (21.2 cm) and 4995 (6.0 cm) MHz confirm Baker's suggestion that 3C 326 is a radio galaxy of unusually large dimensions. The new multifrequency data have also enabled us to determine distributions of spectral index, rotation measure and depolarization over the source as well as the distribution of its magnetic field projected onto the plane of the sky

2. Observations

The WSRT and its operation for continuum observations have been described extensively elsewhere (see e.g. Högbom and Brouw, 1974; Baars and Hooghoudt, 1974). We reduced our observations with the standard reduction package (Brouw, 1971; Weiler, 1973; van Someren Gréve, 1974; Harten, 1975). Before Fourier transformation, the observations (listed in Table 1) were weighted with a Gaussian grading function which decreased in value from unity at the centre of the U-V plane to 0.25 at the longest baseline. Fourier transformation of the resulting data produced synthesized maps of the Stokes parameters I, Q and U. General properties of the maps are given in Table 2. Flux densities are based on the KPW scale (Kellermann et al., 1969); a list of positions and flux densities for calibration sources normally used in Westerbork can be found in Wilson and Weiler (1976).

3. Results

a) 49.2 cm *Wavelength*

In Figure 1a–c we present maps of the total intensity (I), linearly polarized intensity ($(Q^2+U^2)^{1/2}$), polarization position angle ($\frac{1}{2}\tan^{-1} U/Q$) and degree of linear polarization.

The high sensitivity of the present observations reveals one important new feature not seen in earlier synthesis maps (Mackay, 1969): a compact unresolved source situated between the two extended outer lobes. It is connected to the east lobe by a weak bridge of emission, and we identify it with the southern member of the pair of galaxies noted by Mackay (1969) (see Fig. 2a). On the Palomar Sky Survey prints we estimate this galaxy to have a blue magnitude of 18.2 and a red magnitude of 15.7 (the magnitudes should have an accuracy of $\sim \pm\frac{1}{2}$ mag). Similar data for the northern galaxy are 17.7 and 15.0 respectively. Thus both galaxies have rather similar magnitudes and are quite red ($m_b - m_r = 2.7$ and 2.5 for the northern and southern members of the pair respectively). The reddening may well be due to dust in the North Polar Spur. Spoelstra (1972) points out that there is clear evidence that the upper part ($\ell > 60°$) of the spur polarizes starlight, though at lower latitudes ($\ell < 40°$) the situation is more complicated. Since 3C 326 ($\ell = 48°$) lies between these two boundaries no firm conclusion can be drawn but significant reddening within the spur is a possibility. The redshift of this pair of galaxies is 0.0895 (Smith et al., 1976). It is interesting to note that the brighter more northerly galaxy has [O II] and H_α emission lines while the southern one has only absorption line features (Burbidge and Spinrad,

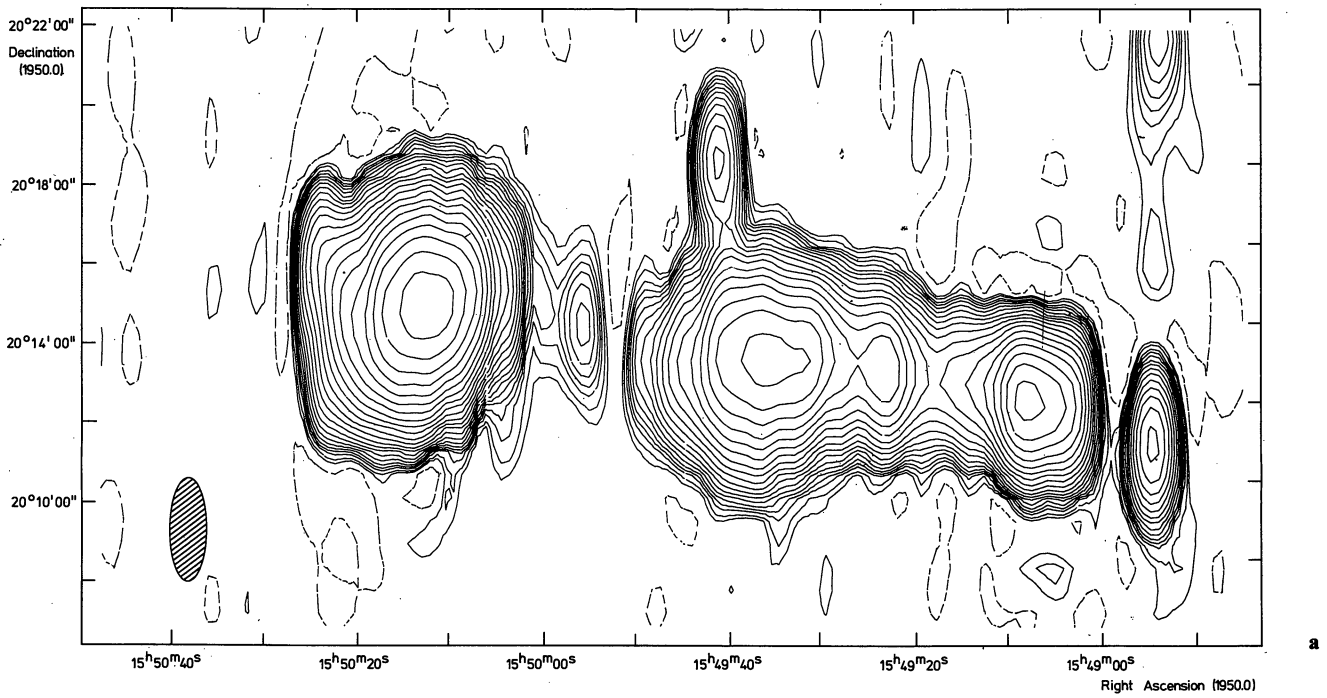

Fig. 1a—c. $\lambda = 49$ cm maps of 3C 326. Shaded ellipses give the half power width of the synthesized antenna pattern. **a** Total intensity: contour levels are -3.5 (dashed), 3.5, 6, 9.5, 12, 15, 19, 23.75, 30, 37.5, 47.5, 60, 75, 95, 120, 150, 190, 237.5, 300, 377.5, 475, 600 and 750 mJy/synthesized beam area. **b** Polarized intensity ($(Q^2+U^2)^{1/2}$): contour values go from 5 to 90 mJy/synthesized beam area in steps of 5 mJy/beam area. Also shown are position angles of the electric vectors. The orientation of the line gives the position angle while the length is proportional to the polarized intensity. **c** Contour of the degree of polarization ($100 \times (Q^2+U^2)^{1/2}/I$). The contours are superposed upon a "radio photograph" of the total intensity

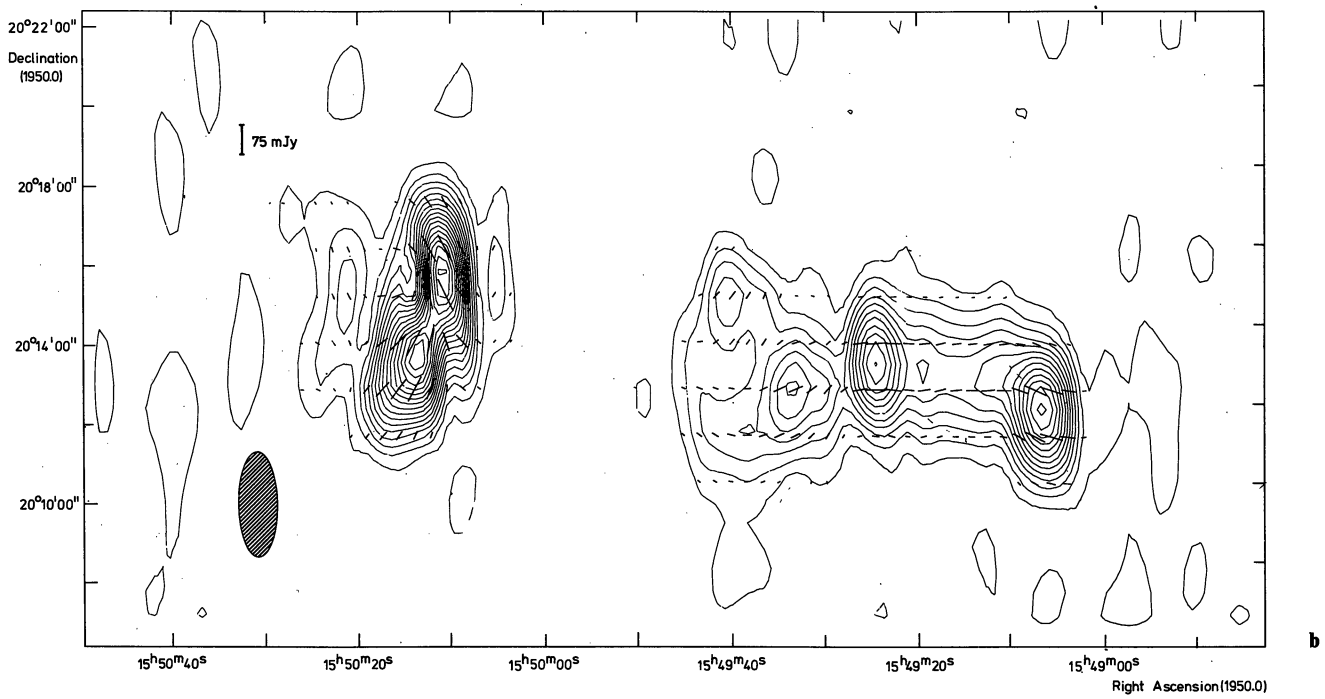

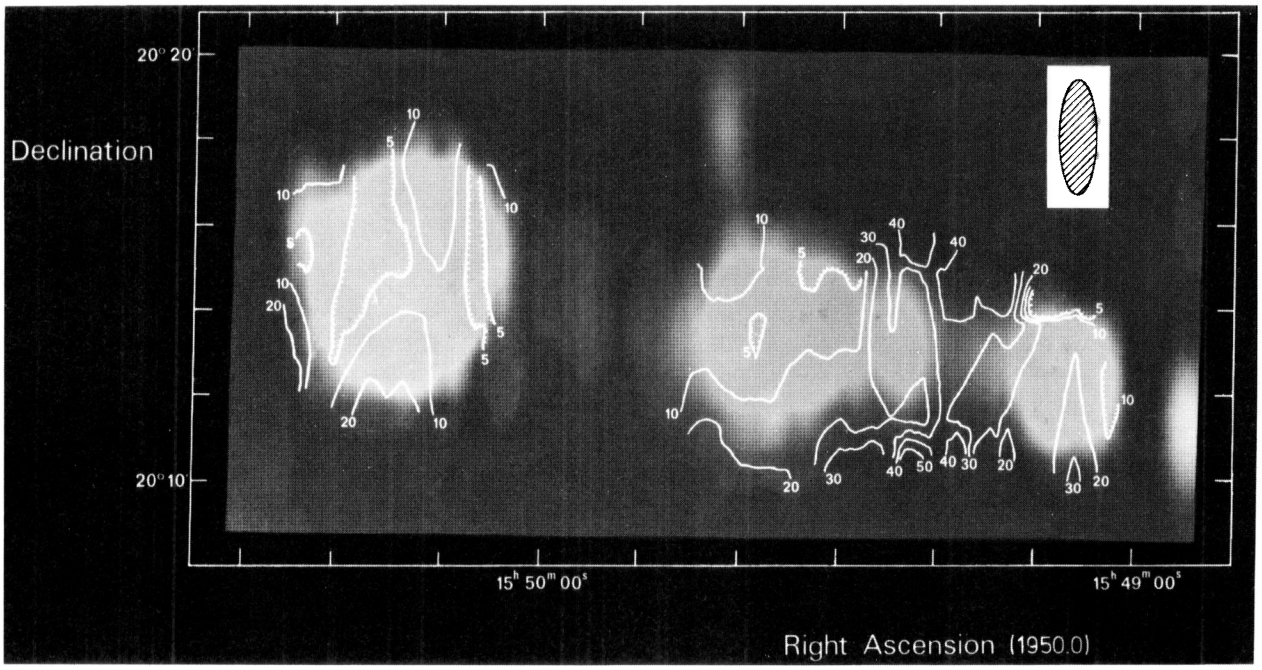

c

private communication). From inspection of the PSS prints we find that the position angle of the major axis of the radio source (~80°) coincides with neither the apparent major nor minor axis of the southern galaxy.

The two other compact sources in Figure 1a are believed to be background sources unrelated to 3C 326.

The degree of linear polarization in 3C 326 (Fig. 1b and c) reaches values as high as 30–40% (at RA $=15^h49^m19^s$, Dec $=20°12'20''$). The distribution of polarized emission (Fig. 1b) has a more complex structure than does the total intensity data which is, at least in part, caused by beam depolarization (see discussion below).

b) 21.2 cm *Wavelength*

Maps of the 21 cm data are presented in Figure 2a–d. The 21 cm observations, with their higher resolution, reveal a more complex structure than was apparent in the 50 cm data. At least five emission peaks are present in the large western component and two in the peculiarly shaped eastern lobe (Fig. 2a). The two outer peaks, A and B, in the western lobe have unresolved gradients at the 21 cm resolution and might be termed "hot spots". Their surface brightnesses are about twice those seen in C and D.

The eastern extended lobe, 1550+20, also has a peak, component G, located at the outer edge. This emission feature is, however, well resolved, having a deconvolved gaussian half width of ~50″ (RA) × 40″ (Dec). Further, its surface brightness is about a factor two less than that seen in the central part of 1550+20.

Note that lines joining components A and G located at the outer ends of the extended lobes and the nuclear source, E, intersect at a position angle of 177.4° ± 1°, so the hot spot alignment with the nuclear source is almost exact.

At 49 cm an emission bridge connects the nuclear source with the eastern radio lobe. In the full resolution 21 cm map this connection is not visible. Part of the reason may be that, unfortunately, the 21 cm map is more dynamic range limited than the 49 cm observation, which may be due to a near undersampling of the sky brightness distribution at 21 cm. The higher resolution 21 cm observations show that the two possible background sources mentioned in the 49 cm discussion are indeed well separated from 3C 326 and presumably unassociated with it.

When one considers the difference in resolution, the 21 cm distribution of polarized intensity is in reasonable agreement with that seen at 49 cm wavelength. The 21 cm polarized structure is quite complex. Although the peaks of polarized emission usually occur close to the brightness peaks in the total intensity map, they are all definitely displaced toward adjacent regions of lower surface brightness. At 21 cm the degree of polarization attains higher values than at 49 cm. The maximum occurs just to the east of component C, and the bridge of emission which connects B to D has an average degree of polarization of between 30 and 40%. This region, while having the highest degree of linear polarization, has, on average, the lowest surface brightness of any part of 3C 326. It also coincides approximately with the part of the source that is highly polarized at 49 cm

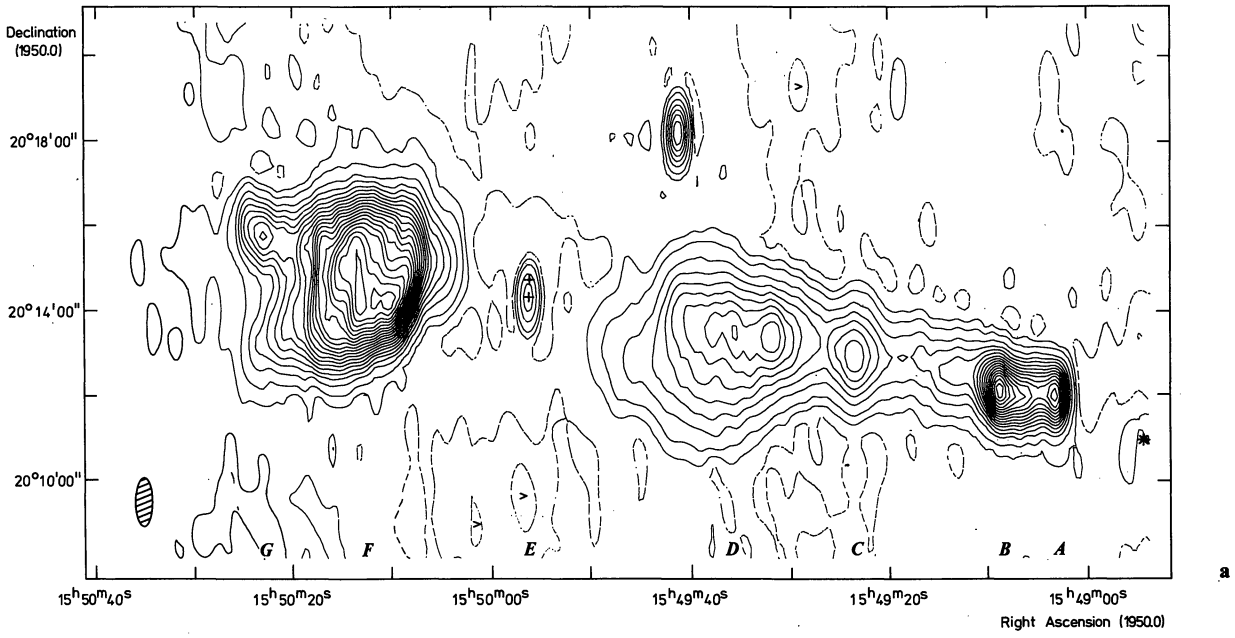

Fig. 2a—d. $\lambda = 21$ cm maps of 3C 326. **a** Total intensity: contour levels are -1 (dashed), 1 and 3.5 mJy/synthesized beam area, and then go from 8.5 to 93.5 mJy/synthesized beam area in steps of 5 mJy/beam area. Each of the letters A-G along the bottom of the map refers to the component of 3C 326 located directly above. Crosses lying within the contours of component *E*, the nuclear source, mark the optical positions of two 15th magnitude (red) galaxies described in the text. The southern galaxy is associated with the radio emission. A "star" at the western end of the map marks the position of a background source which has been subtracted off. **b** Polarized intensity: contour levels go from 1 to 18.5 mJy/synthesized beam area in steps of 1.25 mJy. **c** Position angles of the electric vectors. **d** Contours of the degree of linear polarization superposed upon a "radio photograph" of the total intensity

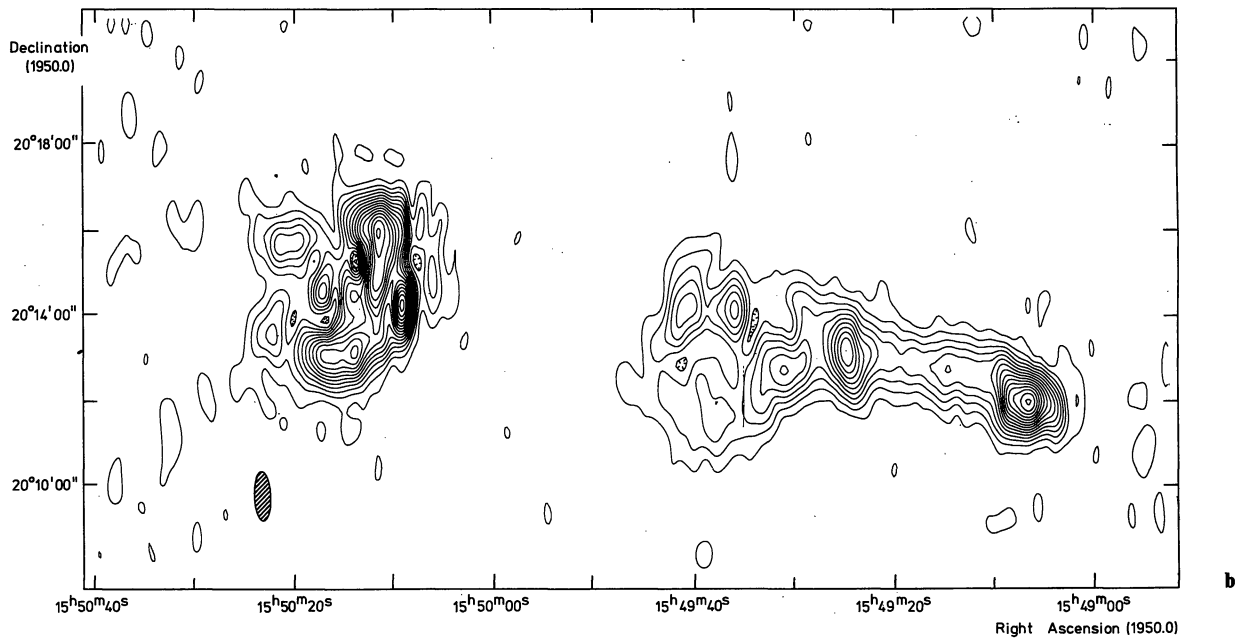

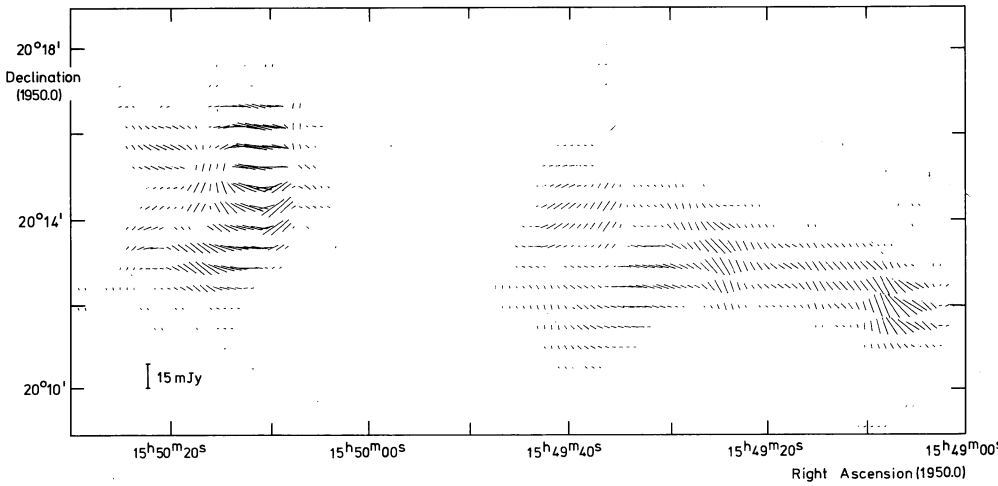

c

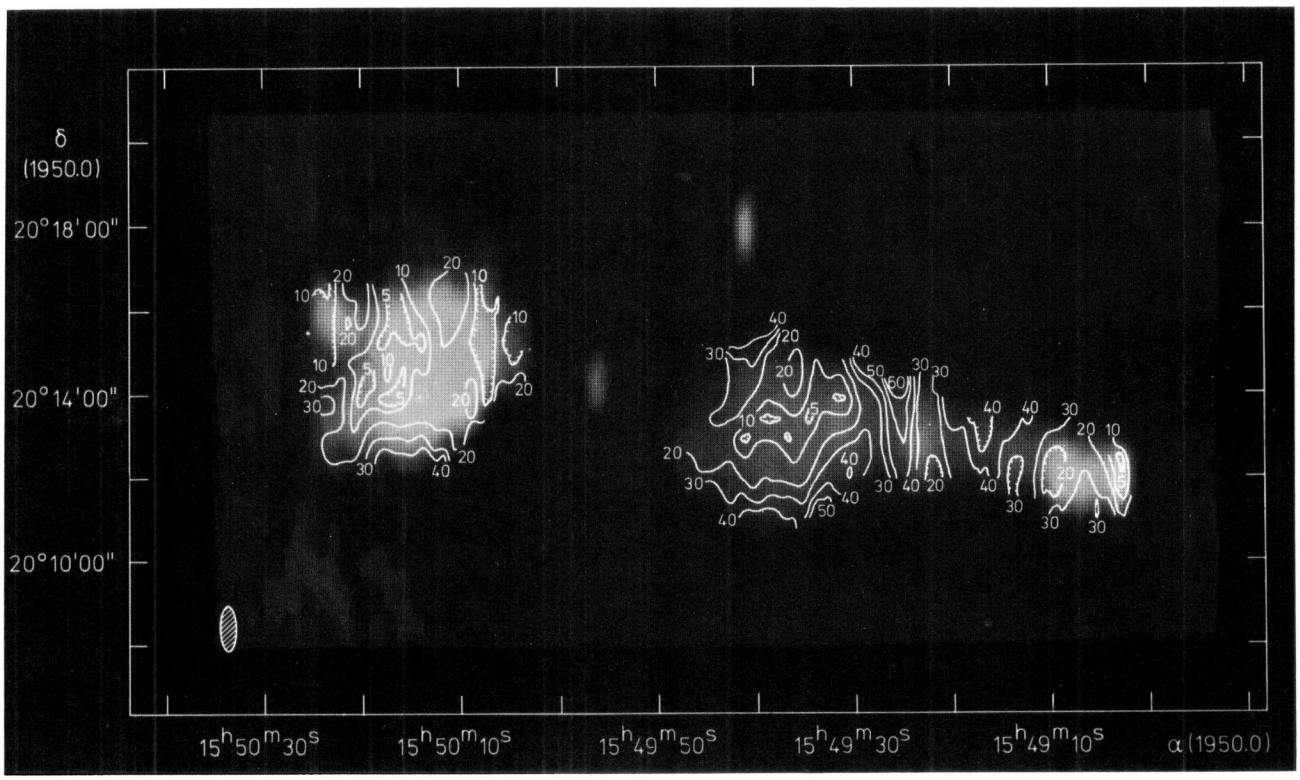

d

wavelength. The two outer western "hot spots" are less highly polarized than is the emission between them. The eastern lobe of 3C 326 has a relatively low degree of polarization.

c) 6 cm *Wavelength*

Separate observations of three parts of 3C 326 have so far been made at 6 cm. The areas studied are (i) the high surface brightness region consisting of components A and B seen at 21 cm, (ii) the central nuclear source and (iii) the eastern lobe. Because the shortest baseline is 900 wavelengths in the *U-V* plane, the 6 cm observations are sensitive only to reasonably compact emission features in the source. Since much of the large scale structure can no longer be detected, we have not attempted to compute integrated parameters (Table 3) from the 6 cm data on the eastern and western lobes.

(i) Components A and B appear nearly unresolved at 21 cm, but in the full resolution (beam 7″ × 20″) 2 × 12 h

Table 3. Measured source parameters for 3C 326

			RA (1950.0)	Dec (1950.0)
Radio position of nuclear source			$15^h49^m56^s.07 \pm 0^s.05$	$20°14'17''.3 \pm 1''.5$
Position of optical galaxy-radio position (arc s)			+0.8	+0.9
	1550+20	1549+20	Nuclear source	Integrated
$S_{49.2}$(Jy)	4.34±0.22	3.12±0.16	0.0238±0.003	7.48±0.38
$S_{21.2}$(Jy)	2.11±0.15	1.46±0.10	0.0186±0.001	3.59±0.25
$S_{6.0}$(Jy)	—	—	0.0132±0.002	—
Spectral index α[a]	− 0.86±0.10	− 0.90±0.10	−0.28 ±0.01	− 0.87±0.10
% Pol. $_{49.2}$	2.8 ±0.2	9.7 ±0.6	<6	2.4 ±0.2
Position angle$_{49.2}$	3.1 ±1.0	92.8 ±1.0	—	92.6 ±1.0
% Pol.$_{21.2}$	7.0 ±0.6	12.6 ±1.3	<5	7.9 ±0.7
Position angle$_{21.2}$	77.1 ±1.1	45.0 ±5.6	—	59.0 ±4.4
Rotation measure[b]	25.4 ±0.1	20.2 ±0.5	—	18.9 ±0.4

[a] α defined as $S \propto \nu^{\alpha}$. For the nuclear source α has been determined from the flux densities at all three wavelengths but in the other cases it is based solely on the 21 and 49 cm data

[b] Rotation measure of 1550+20 determined after inclusion of data from Baker (1974) and Gardner et al. (1975)

6 cm map (Fig. 3) thay are almost completely resolved out. Most of the detected 6 cm emission comes from an extended feature, although one unresolved component (at RA = $15^h49^m03^s$, Dec = 20°12′15″) remains. This component has a 6 cm peak flux density of ~6.3 mJy, part of which, ~2 mJy, may be contributed by the surrounding low surface brightness plateau. An enhanced emission region, located at RA ~$15^h49^m06.1^s$, Dec ~20°11′54″ occurs in what, at 21 cm resolution, is a bridge joining the two high surface brightness features. It is, however, well resolved, having a deconvolved gaussian half power width of ~9″ (RA) × 23″ (Dec). Linear polarization detected in this component is unresolved, and located ~4″.5 to the southeast (position angle = 165°) of the total intensity peak. The polarized intensity is 4±0.7 mJy and thus the degree of polarization is 80±20%. The position angle is 160±10°. Some polarized flux also occurs in the area surrounding this feature since convolution to 21 cm resolution causes the peak polarized flux density to increase to 7.5±1.25 mJy. The degree of polarization drops to 27±5% so the surrounding region probably has a much lower intrinsic degree of polarization. It is also of interest to note that the unresolved feature mentioned above coincides with a ~3σ peak (~2.5 mJy) in the polarized intensity map. Thus this feature, too, may be highly polarized (up to 40%) but the signal is not strong enough to be fully confident of the measurement.

(ii) The central nuclear source appears to be still unresolved at 6 cm so its angular size is < ~4″.

(iii) Due to telescope failure it was possible to observe the eastern lobe of 3C 326 for only a 1 × 12 h period at 6 cm wavelength. Component G in the 21 cm map is almost completely resolved out in the full resolution map at 6 cm (Fig. 4). There are only two 3σ deflections visible near this position. Considerable fine scale

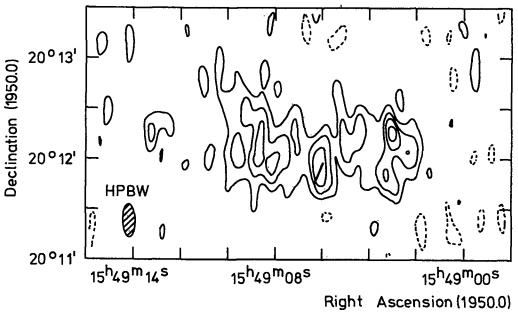

Fig. 3. A 6 cm full resolution map of the region comprising components A and B in Figure 2a. The contour levels are −1.5 (dashed), 1.5, 3, 4.5 and 6 mJy/synthesized beam area. The orientation of the bar at RA = $15^h49^m06^s.2$, Dec = 20°11′50″ indicates the electric vector position angle of the polarized emission detected there and discussed further in the text

structure is, however, detected in the position of the centre of the lobe. Some of the emission regions have sizes of several beamwidths, but other components appear unresolved. From planimetry, we find the total flux density detected in the full resolution map that is contained in the lowest drawn contour (2.25 mJy/beam area) to be 270±85 mJy. We estimate the zero spacing integrated flux density of this lobe of 3C 326 to be ~725 mJy at 6 cm (see discussion in Section 4a on spectra). Thus ~37±12% of the flux from the eastern component originates in relatively compact structures. A 6 cm map of this component with better signal to noise ratio is, however, definitely necessary before one can properly relate the observed structure to that seen in the lower resolution 49 and 21 cm maps.

No polarized flux is detected from the eastern lobe in the full resolution 6 cm map.

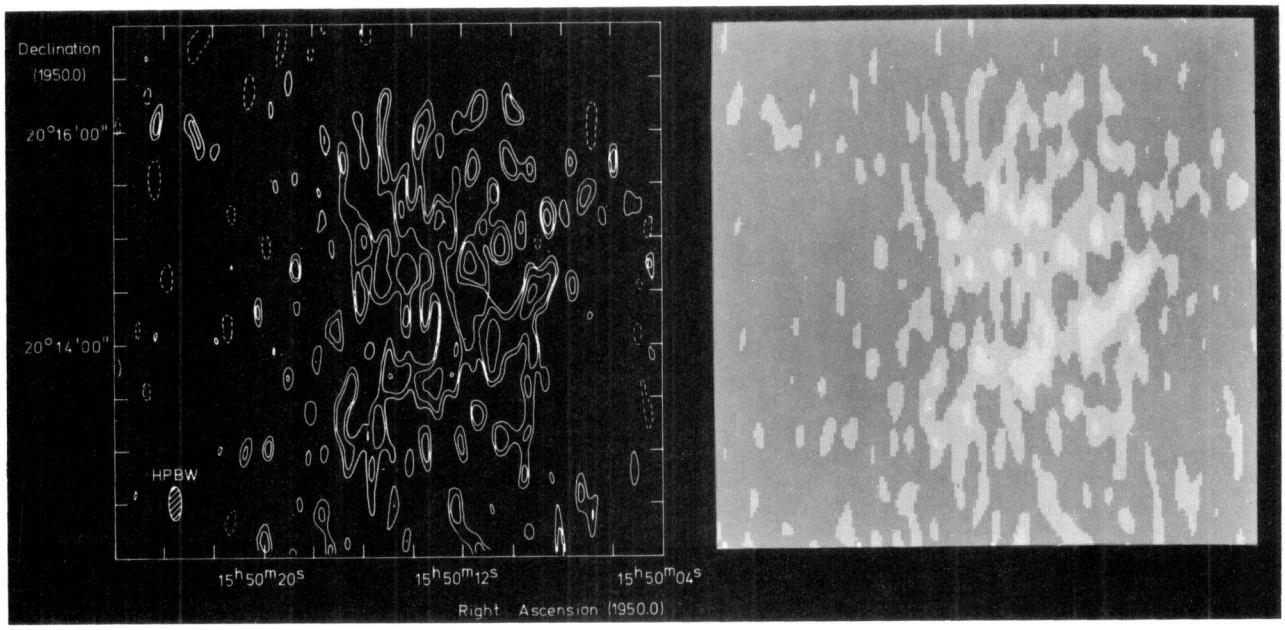

Fig. 4. A 6 cm full resolution map of 1550+20, the eastern component of 3C 326. The contour levels are −2.25 (dashed), 2.25, 3, 4.5 and 6 mJy/synthesized beam area. As an aid to the eye a "radio photograph" of the emission is displayed adjacent to the contour map

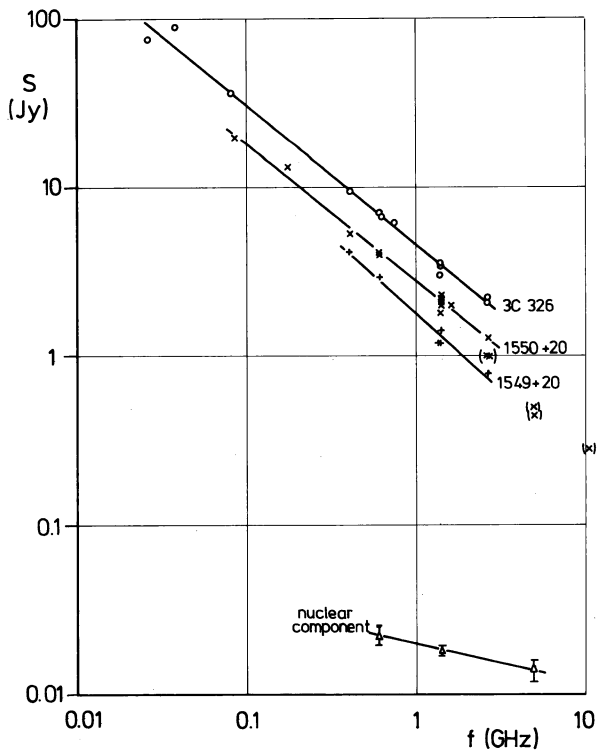

Fig. 5. The radio spectrum of the integrated emission from 3C 326 and its components. Data are taken from Dickel et al. (1967), Höglund (1967), Smith (1968) as reported by Readhead and Hewish (1974), Shimmins and Day (1968), Mackay (1969), Kellerman et al. (1969), Artyukh et al. (1969), Bridle et al. (1972), Baker (1974), Gardner et al. (1975), Viner and Erickson (1975) and Table 3 of this paper. The data have been adjusted to the flux density scale derived by Véron et al. (1974) as described in the text

4. Source Properties as a Function of Wavelength

Comparison of the observed spatial distribution of total and polarized emission from radio sources as seen at different wavelengths can yield important clues as to intrinsic source properties.

a) Spectrum of the Integrated Emission from 3C 326

Table 3 lists our values of integrated flux density and polarization for the components of 3C 326. The spectral indices given in the table have been computed using only the flux densities listed. Figure 5 is a plot of the flux densities that have been measured for 3C 326 at different frequencies. To facilitate the comparison, we have applied the correction factors derived by Véron et al. (1974) to all the plotted points. For the Westerbork measurements the Véron et al. factors for KPW have been applied to the flux densities in Table 3.

The integrated spectrum of 3C 326 appears to obey a simple power law with spectral index $\alpha = -0.82 \pm 0.02$ (the error has been calculated simply from the unweighted least squares fit to the data) between 26 and 2700 MHz. There are no integrated flux density measurements of the entire source available at higher frequencies. 1550+20 has a power law spectrum with $\alpha = -0.81 \pm 0.03$ over the range 86 to 2700 MHz. At higher frequencies, the single dish measurements (made with the Bonn 100 m, Parkes 64 m or NRAO 43 m telescopes) would indicate a considerable steepening in the spectrum of 1550+20, especially at frequencies of 5000 MHz and

higher. However, analysis of our own 21 and 6 cm data (see next section) indicates that the spectral index of 1550+20 is still ~ -0.9 (KPW scale) to at least 5000 MHz. The most likely explanation for the discrepancy is that the single dishes are beginning to resolve this lobe and that the reported measurements, which are mostly peak flux densities, underestimate the total flux density. We believe the correct integrated 6 cm flux density to be 700–750 mJy.

Direct measurements of the western component, 1549+20, are sparser, but its spectrum also follows a power law with $\alpha = -0.92 \pm 0.06$ between 408 and 2700 MHz. The small difference in spectral index between 1549+20 and 1550+20 is probably insignificant, especially when one considers the relatively small frequency interval over which that for the former was calculated, and the fact that the spectral index of the latter is virtually identical to that of the entire source. The spectrum of the nuclear component is considerably flatter than that of the rest of the source (see Table 3). For comparison with the values quoted above, its spectral index is $\alpha = -0.22 \pm 0.02$ if the flux densities given in Table 3 are also corrected with the Véron et al. factors.

b) Spectral Index Distribution over the Source

We determined the spectral index distribution over 3C 326 between 49 and 21 cm by intercomparing the 49 cm map with one at 21 cm convolved to the 49 cm resolution. A one dimensional cross-cut through the spectral index map at position angle 80°, approximately along the source's major axis, is shown in Figure 6. We have not shown a two-dimensional map since the 49 cm resolution is $\sim 160''$ in declination and thus 3C 326 is effectively a one dimensional east-west source, especially that part to the west of RA = $15^h49^m30^s$.

The conclusions that may be drawn from Figure 6 are (1) that there is no significant change in spectral index over the eastern lobe. It should be noted that, because of dynamic range limitations in the 21 cm map, it is not possible to say anything quantitative about the spectral index of the emission bridge seen at 49 cm between the nuclear source and component F. (2) The spectral index becomes systematically flatter over the western lobe as the distance from the nuclear source increases. The variation in the western lobe is, however, quite small and certainly, considering the errors of $\sim \pm 0.07$ associated with each sample point, not more than ~ 0.3.

Our conclusions concerning the spectral index distribution between 49 and 21 cm are reinforced by the results from intercomparison of 6 cm maps (convolved to the 21 cm resolution) with the 21 cm ones. Figure 7 shows the distribution of spectral index between 21 and 6 cm along a cross-cut in position angle 67° through the eastern lobe of 3C 326. It is clear that between 21 and 6 cm there is no change in spectral index over the source.

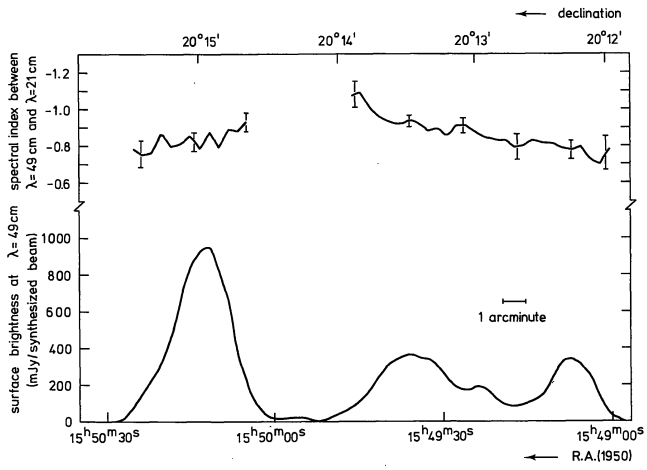

Fig. 6. A cross cut along the major axis of 3C 326 in position angle 80° showing the 49–21 cm spectral index distribution over the outer lobes as a function of position. Error bars are plotted at representative sample points. For reference a cross cut through the $\lambda = 49$ cm total intensity is also drawn

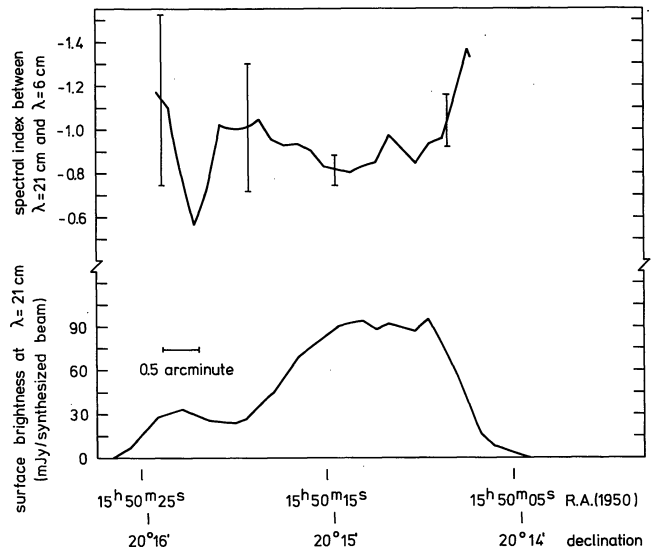

Fig. 7. A cross cut through 1550+20 in position angle 67° showing the 21 – 6 cm spectral index as a function of position. Error bars are plotted at representative sample points. For reference a cross cut through the $\lambda = 21$ cm total intensity map is also drawn

Further, the average spectral index between 21 and 6 cm appears to be -0.9, in excellent agreement with the integrated value of -0.86 found between 21 and 49 cm (Table 3).

Thus the spectral properties of the eastern lobe may be summarized as follows: (1) there are no significant variations in spectral index over the lobe; and (2) the integrated spectrum appears to obey a simple power law with a spectral index of -0.82 (Véron et al. scale) from very long metre wavelengths down to at least 6 cm.

The situation regarding the spectral index of the region comprised of components A and B is not quite so clear cut. A comparison of 21 and 6 cm maps with similar resolution yields a mean spectral index of -0.59 with maximum deviations of ± 0.06 in the region lying between $15^h49^m03^s$ and $15^h49^m10^s$. Since the r.m.s. error at a "typical" sample point is computed to be ~ 0.06, there are no significant changes from the mean value. However the 49–6 cm spectral index of the single peak seen on maps with similar resolution is -0.71 ± 0.03. Further, recall that the spectral index between 49 and 21 cm is about -0.78 ± 0.05 in this area (Fig. 6). We are thus faced with two alternatives: (1) that the 21 cm flux densities are systematically too low; or (2) that the spectrum of this region is systematically flatter between 21 and 6 cm than between 49 and 21 cm.

(1) The maximum instrumental effect, if corrected for, would cause the 49–21 cm spectral index to increase by ~ 0.03 and the 21–6 cm spectral index to decrease by about the same amount. The 49–21 cm and 21–6 cm spectral indices would then differ by only 1.7 σ, which is no longer significant.

(2) However, the difference could be real. This would imply curvature in the spectrum of emission from the region which includes components A and B. The effect could be enhanced by the fact that the 21 and 6 cm maps with similar *U-V* coverage are sensitive to relatively compact features which might have a rather flat spectrum while the 49–21 cm maps of similar *U-V* coverage may be sensitive to an additional low spatial frequency component having a steeper spectrum. It is possible that the concave shape is the result of merely summing two straight spectra with different slopes. However, the present measurements at all three frequencies do confirm that the spectrum of components A and B is flatter than that of 1549+20 as a whole, i.e. the spectrum of the entire lobe steepens as one goes eastwards from A and B.

c) Polarization Data

One important datum that can be derived from polarization measurements is the projected direction of the magnetic field perpendicular to the line of sight, since synchrotron radiation is polarized perpendicular to the direction of the field. Before this is possible one must derive the rotation measure (*RM*) over the source.

After combining our 49 and 21 cm integrated position angles with the measurements of Baker (1974) and Gardner et al. (1975) we derive an integrated *RM* of 25.4 ± 0.1 rad m^{-2} for 1550+20, with due allowance for $n\pi$ ambiguities in the position angles. This *RM* agrees with the value of 24 ± 3 computed by Vallée and Kronberg (1975). Gardner et al. (1975) list short wavelength polarization measurements on three other sources near to 3C 326; 1545+21, 1547+21 and 1553+20 (3C 326.1). The observations of these three sources are most simply described by rotation measures of 21, 37 and 61 rad m^{-2} respectively, so a small positive *RM* seems appropriate at this galactic latitude and longitude.

Then, from our 49 and 21 cm convolved data, rotation measures at the individual data sampling points on 1550+20 were computed under the conditions that (1) the *RM* be small and positive, (2) there be no abrupt changes in *RM* at sampling intervals smaller than the half power beamwidth and (3) the individual rotation measures be consistent with an integrated value of +25 rad m^{-2}. The result, shown in Figure 8, is that the *RM*'s in 1550+20 have values lying between 22 and 29 rad m^{-2}. The *RM* systematically increases from the lower to the higher value as one moves from south to north over the lobe. (Note that the *RM*'s of +32 rad m^{-2} found just to the northeast of the centre of 1550+20 are probably not significant. They occur in an area which has a very low degree of polarization at both 49 and 21 cm—see Figs. 1c and 2d—and thus the electric vector position angles used to derive the *RM* become very uncertain.)

The situation concerning 1549+20 is complicated by the fact that there exist no single dish polarization observations of this lobe in the literature. Under condition (1) above, it is found that the integrated polarization data in Table 3 are most likely described by rotation measures of either +36, 20 or 4 rad m^{-2}. Further, under the constraint of condition (2) above, it is found that all the sample points have rotation measures lying within 5 rad m^{-2} of whatever is the correct integrated value. Convolution of the 6 cm data on the far western end of this lobe to the 49 cm resolution gives a result that is only consistent with an integrated *RM* of ~ 20 rad m^{-2}.

The resulting distribution of *RM* over this lobe is also shown in Figure 8. It is everywhere within ± 2 rad m^{-2} of 20 except in the northeastern corner where it is systematically lower by -2 to -5 rad m^{-2}.

With these *RM*'s we have derived the electric vector intrinsic position angles. Rather than use these position angles, we have plotted, in Figure 9, the orthogonal to the electric vector position angles, which should indicate the direction of the component of magnetic field in the source perpendicular to the line of sight.

In 1549+20, especially at right ascensions west of $\sim 15^h49^m30^s$, the magnetic field is essentially aligned along the source axis.

The situation regarding that part of 1549+20 lying to the east of $15^h49^m30^s$ is more complicated. In the southern area the magnetic field tends to follow the outline of the source and is tangentially aligned with the contours of equal total intensity. However the northeastern area that had the anomalous *RM* also has a magnetic field orientation that contrasts with that seen in the surrounding area. The field appears directed north-south here and thus perpendicular to the total intensity contours and to the magnetic field in the surrounding region. It is then clear that the lower degree

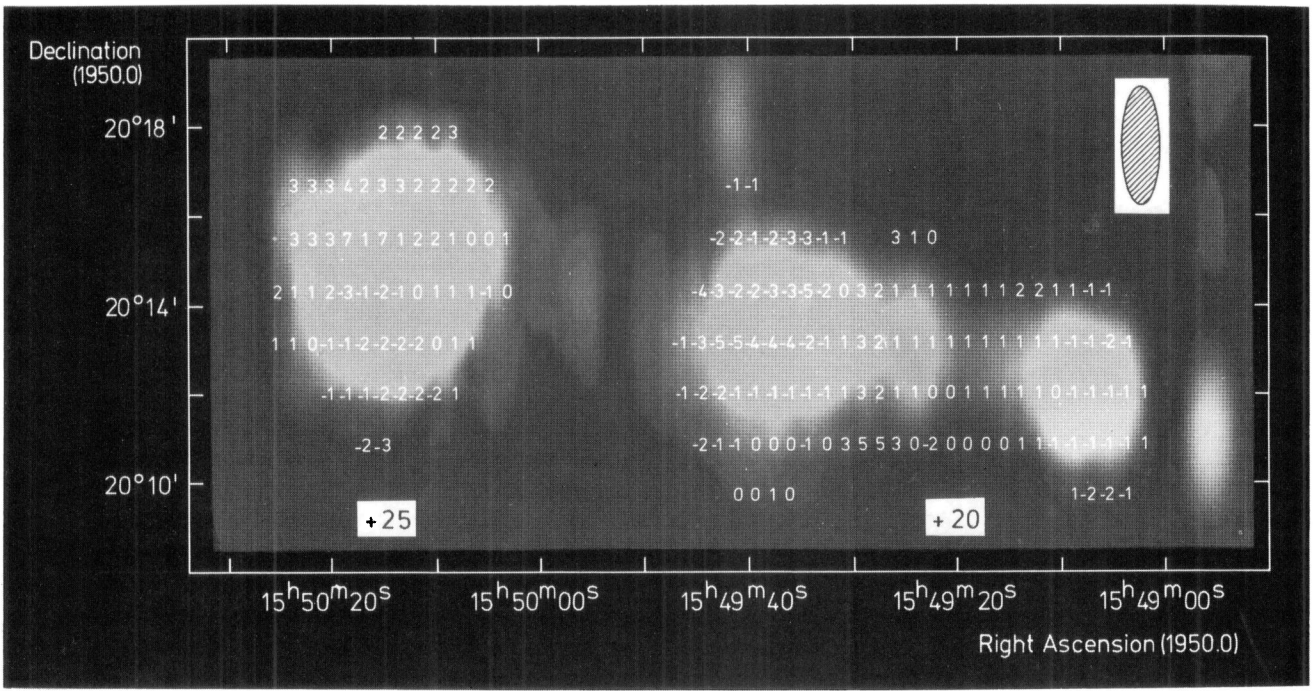

Fig. 8. The distribution of rotation measure over 3C 326 as computed from the 49 cm and 21 cm convolved data superposed upon a "radio photograph" of the 49 cm total intensity. Note that to produce a simple grid of single digit numbers we have subtracted integrated rotation measures, whose derivation is described in the text, of $+25$ rad m^{-2} and $+20$ rad m^{-2} from the values measured at individual sample points in the east and west components respectively. For reference, these integrated values are displayed under each component

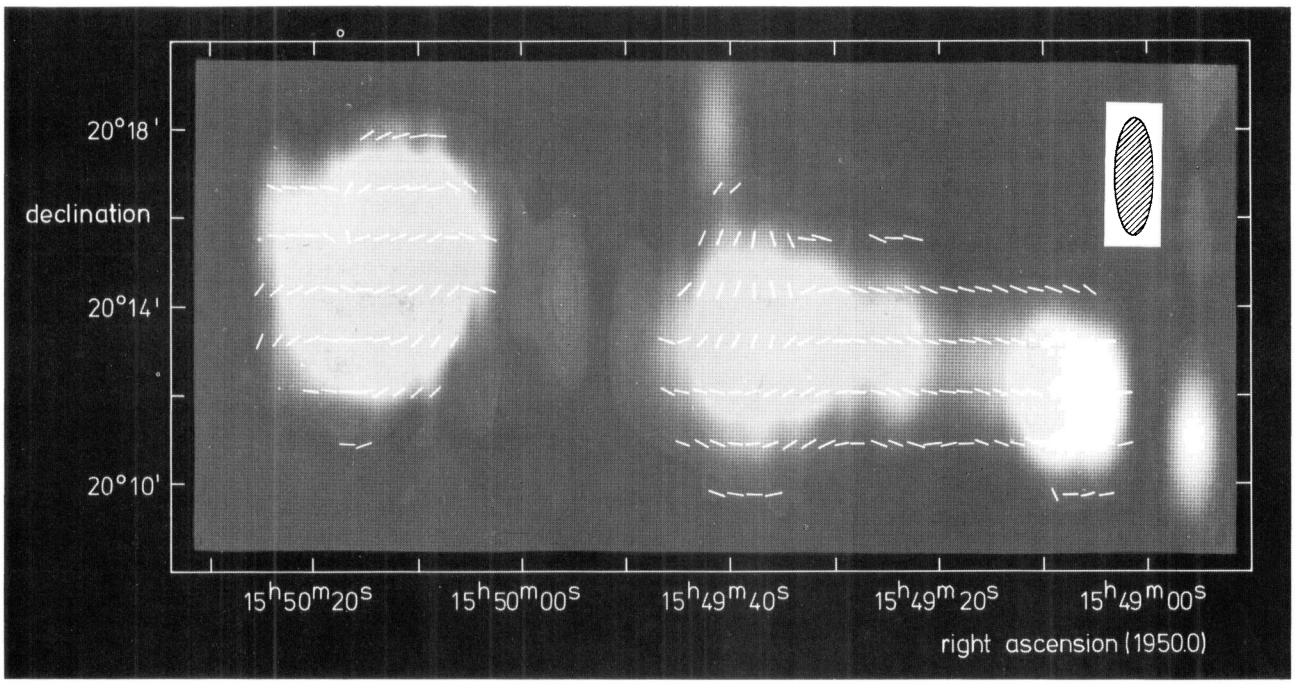

Fig. 9. The direction of the magnetic field in 3C 326 projected perpendicular to the line of sight. The white bars representing the field vectors are superimposed upon a "radio photograph" of the 49 cm total intensity distribution

Table 4. Some physical parameters of 3C 326

Redshift		0.0895 (Smith et al., 1976)			
Luminosity distance ($H_0=75$, $q_0=0.5$)		365 Mpc			
Angular extent		19'.5			
Projected linear extent		1.7 Mpc			
Size conversion ratio		1.49 kpc arc s^{-1}			
	1550+20	1549+20		Nuclear source	Total (t) or mean (m)
		E[a]	W[a]		
Major axis (kpc)	477	436	524	<6	—
Minor axis (kpc)	429	409	83	—	—
Major axis position angle (°arc)	~135	~ 90	~ 78	—	—
Volume (10^{72} cm^3)[b]	1.4	1.1	0.055		
P_{49}(10^{25} W Hz^{-1})	6.9	4.9		0.036	11.8 (t)
P_{21}(10^{25} W Hz^{-1})	3.3	2.3		0.028	5.7 (t)
L(10^7-10^{10} Hz) (10^{42} erg s^{-1})	2.7	2.0		0.022	4.7 (t)
E_{min}(10^{59} erg)[c]	3.4	2.6		—	6.0 (t)
H_{eq}(μG)[c]	1.6	1.6		—	1.6 (m)
Energy density (10^{-13} erg cm^{-3})	2.5	2.2		—	2.5 (m)

[a] E: RA > 15^{h}49^{m}27^s.5; W: RA < 15^{h}49^{m}27^s.5

[b] Calculated assuming that each component is a prolate spheroid

[c] Equipartition parameters, calculated assuming that the energy contained in protons equals that of the relativistic electrons, and using the spectral indices in Table 3

of polarization seen in the centre of the component as compared to that detected in the outer part is caused by beam depolarization and vector cancellation.

The magnetic field in 1550+20 exhibits complex behaviour that is generally related to the total intensity distribution seen in the 21 cm full resolution map, even though the data have been studied with the 49 cm resolution. In the most northerly part, and in the south and southwest the field appears circumferentially aligned. In the centre and at the western edge the field is aligned in position angle ~90°, which is quite close to the direction of the major axis of 3C 326. The east-west alignment at the western edge of the lobe may be connected with the fact that, at 49 cm, we see a bridge connecting this part of the lobe with the central source. In the northeast and southwest corners the field aligns roughly with the directions of the projections or spurs of emission that at 21 cm full resolution are seen to jut out from the main body of the lobe.

In the region around RA ~ 15^{h}50^{m}17^s.5, Dec ~20°15'30" the magnetic field vectors rapidly change orientation. This suggests, again, that the low percentage polarization seen in this locale is at least in part caused by beam depolarization and vector cancellation.

d) Computation of Physical Parameters

Tables 4 and 5 list various physical properties calculated for 3C 326. The luminosity distance to the source was computed from the redshift with the assumption that $H_0=75$ km s^{-1} Mpc^{-1} and $q_0=0.5$. The energy, energy density and magnetic field were calculated, assuming equipartition, with the standard synchrotron equations (e.g. Pacholczyk, 1970, Chapter 7), and using the condition that the heavy particle energy is equal to that of the relativistic electrons. For calculating the volumes of the components we assumed them to be prolate spheroids having the major and minor axes listed in the Table. The total radio luminosities of the components have been calculated with the assumption that the radio spectra of all the components are optically thin and radiate between 10^7 and 10^{10} Hz.

The thermal electron density and total mass contained within the components were calculated from the depolarization observed between 21 and 49 cm. Figure 10 is a cross-cut in position angle 80°, where we show the degree of polarization at 49 and 21 cm and the depolarization between these two wavelengths. We define the depolarization as

$$\frac{\text{percentage polarization at the longer wavelength}}{\text{percentage polarization at the shorter wavelength}}$$

We have only plotted the one dimensional strip scan rather than a two dimensional map of the depolarization since (1) the source is essentially one dimensional with the 49 cm resolution, and (2) the diffuse lobes to the east of 15^{h}49^{m}30^s have rather low percentage polarizations and consequently the depolarization parameter has a large error at individual sample points (errors at representative data points are plotted in Fig. 10). Consequently one is mainly concerned with "average" conditions within

Table 5. Physical parameters of the region containing components A and B

S_{49}	~800 mJy
S_{21}	~410 mJy
Major axis	~158 kpc
Minor axis	~ 40 kpc
$L(10^7-10^{10}$ Hz)	$5.0\ 10^{41}$ erg s^{-1}
H_{eq}	5.0 μG
E_{min}	$9.4\ 10^{57}$ erg
Energy density	$2.4\ 10^{-12}$ erg cm^{-3}

these lobes rather than a detailed map. The one dimensional scan thus serves our purpose adequately.

Changes in the observed degree of polarization between 21 and 49 cm could occur if the *RM* changed considerably within one half beamwidth element of resolution. From Figure 8, the maximum change of *RM* in 1549+20 within a half beamwidth sampling interval is about 3 rad m^{-2}. This value means that a relative change in position angle of up to ~34° would occur within one half beamwidth between 21 and 49 cm. This change in position angle could cause the observed degree of polarization to change by up to ~±20% between the two wavelengths, and thus produce the wild fluctuation in the depolarization centred at RA ~15^{h}49^{m}34^s, Dec ~20°13′20″, where the *RM* (Fig. 8) is indeed changing value by ~3 rad m^{-2}. Consequently we have only related internal conditions within the source to the average depolarization seen in each lobe. A reasonable estimate for the average depolarization between 49 and 21 cm in the eastern lobe is, considering the uncertainties, ~0.75. That in the western lobe would seem to be slightly higher, an average being ~0.85.

Burn (1966) has related the observed depolarization to intrinsic conditions within a radio source, under the assumption that the depolarization is due to ionized thermal electrons intermixed with the magnetic field inside the source. If we assume the source to be approximated by Burn's slab model, the depolarization as a function of wavelength is

$$1-\frac{(KnH_zL\lambda^2)^2}{6}\cong\frac{P_\lambda}{P_i}=\text{depolarization}, \qquad (1)$$

where P_λ=degree of polarization at wavelength λ, P_i=intrinsic degree of polarization at 0 wavelength, L=pathlength through source, H_z=magnetic field component parallel to the line of sight through the source, n=number density of ionized thermal electrons and K=a constant, which in cgs units is $2.62\ 10^{-17}$.

To derive n, the density of ionized thermal material, we make the further assumption that the pathlength through the source is equal to the size of the source's minor axis. We must also have a value for H_z and P_i. We can use the degree of polarization in the 21 cm full resolution map as an estimate of P_i if we are sure that

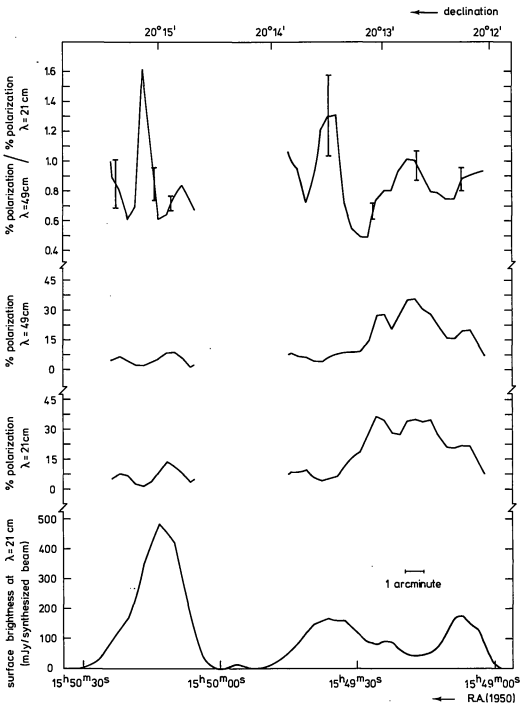

Fig. 10. Cross-cuts along the major axis of 3C 326 showing the depolarization over the outer lobes as a function of position. Error bars are plotted at representative sample points. (Note that the deflection of 1.6 just to the left of 20°15′ is not significant, this data point having an uncertainty of ±1.2.) Also plotted for reference are the degree of polarization at 49 cm and the 21 cm degree of polarization and total intensity, both of which have been convolved to the 49 cm resolution. Typical uncertainties in the degrees of polarization are ±1–2%

the source has not begun to depolarize by 21 cm. We check if this is the case by looking at the degree of polarization in the 6 cm maps convolved to the 21 cm resolution. No significant polarization is detected in the eastern lobe of 3C 326, which implies that the degree of polarization in the centre of the lobe is ≦~18%. This value agrees well with the measured 21 cm value of ~15% (Figs. 2d and 10) in the centre of the lobe. When the 6 cm map of the far western end of the preceding lobe is convolved to 21 cm resolution components A and B are seen. The degree of polarization in the bridge connecting them is ~27±5%, which again agrees very well with the observed value of ~30% in the 21 cm map (Fig. 2d) of the area.

H_z, the component of the magnetic field along the line of sight, was calculated from Burn's (1966) Equation (31). For 1549+20 the value of H_z used in the computation may be an overestimate since the field mostly runs directly along the source and, considering the large size of the component, one expects little foreshortening. Table 6 lists the values of H_z and the values for n then derived from Equation (1) as well as an estimate of the total mass contained within the radio lobes. Also included in Table 6 is the resulting Alfvén

Table 6. Parameters derived from the 21–49 cm depolarization

		1549+20	
	1550+20	Component D	Region containing components A and B
Intrinsic degree of polarization (%)	~10	~30	~30
H_z (Gauss)	$3.5\ 10^{-7}$	$5.7\ 10^{-7}$	$1.9\ 10^{-6}$
Depolarization between 21 and 49 cm	~0.75	~0.85	~0.85
Line of sight depth through source (kpc)	429	409	40
Thermal electron density (cm^{-3})	$4.2\ 10^{-5}$	$2.1\ 10^{-5}$	$6.5\ 10^{-5}$
Total mass ($\mathcal{M}_\odot$)	$4.8\ 10^{10}$	$2.0\ 10^{10}$	$2.1\ 10^{8}$
Alfvén speed (km s^{-1})	$5.5\ 10^{2}$	$7.5\ 10^{2}$	$1.4\ 10^{3}$
|Internal rotation measure| (rad m^{-2})	5	4	4

speed in the components. Note that the thermal gas density could still be underestimated. Use of Equation (1) involves the assumption that H_z is constant along the line of sight. If there are field reversals, then the average gas density would be underestimated by a factor $n^{-1/2}$, where n is the number of field reversals along the path-length through the source (Longair et al., 1973). However, where the degree of polarization is 20% or more, n is unlikely to exceed 10.

Now the rotation measure equals KnH_zL so, using the parameters listed in Table 6, we have typical *RM*'s intrinsic to the source of ~5 rad m^{-2} (1550+20) and ~4 rad m^{-2} (1549+20). One cannot determine the sign of the *RM* without knowledge of the vector direction of H_z within the components. The fluctuations of *RM* seen in Figure 8 obviously indicate either a change in characteristics internal to the source or foreground galactic effects. Since the average *RM* intrinsic to the source is quite low, fluctuations of 1 or 2 rad m^{-2} might easily reflect fluctuations in the line of sight magnetic field component, thermal electron density or the line of sight depth by factors of 20–30%, which would be entirely reasonable. For instance, the systematic negative residual *RM* seen in the northern part of component D correlates well with the presence of a magnetic field whose projected direction perpendicular to the line of sight is clearly different to that of the magnetic field in the rest of 1549+20. We can infer that the strength of the component parallel to the line of sight is also probably different to that in the remaining part of 1549+20, causing the change in the observed *RM*. If n and L still retain approximately the values listed in Table 6 for component D, then a residual *RM* of -3 rad m^{-2} implies a differential magnetic field component of $-4\ 10^{-7}$ G along the line of sight with respect to conditions elsewhere in 1549+20.

The changes in *RM* in 1550+20 do not correlate especially well with variations in the observed magnetic field direction. Thus the systematic increase in *RM* from south to north over the component could be either a foreground effect due to our galaxy or might hint at a systematic change in the projected line of sight component of the magnetic field, being directed away from us in the south and toward us in the north.

5. Discussion

With an angular size of 19.″5 and a redshift of 0.0895 (Smith et al., 1976) 3C 326 has a intrinsic size, projected perpendicular to the line of sight, of 1.7 Mpc ($H_0=75$ km s^{-1} Mpc^{-1}). Thus it is the second largest radio galaxy yet discovered. Only 3C 236 (Willis et al., 1974), with a projected linear diameter of 3.8 Mpc ($H_0=75$), is larger. The radio luminosity, equipartition energy and magnetic field strength of 3C 326, listed in Table 4, are roughly comparable with the values measured in 3C 236 (see Table 3 of Willis et al., 1974). However we postpone a detailed intercomparison of the very large radio galaxies until the multifrequency studies of the other ones are completed.

In a recent review, De Young (1976) has discussed three current mechanisms for transporting energy from the nucleus of the central galaxy to the outer radio lobes: (a) continuous flow of relativistic fluid; (b) expulsion of extremely compact objects; (c) ejection of plasma clouds by explosive outbursts. Variations of such models appear to be designed to tackle major features of strong radio sources: their double structure and alignment with the central galaxy; the high degree of collimation and confinement of the components; the need for supplying energy to the outermost regions in a nearly lossless way. Many of the features of these models concern the initiation of energy flow within the nucleus and its outward transport. Our angular resolution being insufficient to study the nuclear region (except to say that an unresolved component does coincide with the central galaxy), and the outward energy transport being (to the extent that it is lossless) unobservable, we must content ourselves with considering what the observations of 3C 326 tell us about the energy after it is deposited in the extended components.

However, we can reiterate (Section 3b) the high degree of alignment between the central component and the outer hot spots seen in the 21 cm map (Fig. 2a). While such alignment is readily achieved by mechanism (b), for mechanism (a) it means that the relativistic beams must be stable over distances exceeding 1 Mpc, while for mechanism (c) it implies that the mean outward motion of the radio components must be much greater than the speed of the galaxy through any sur-

rounding medium. We note in passing that the outer "hot" spots in Figure 2a are largely resolved with the 6 cm beam (Figs. 3 and 4) and no features comparable to the high surface brightness components of Cygnus A are seen. Nevertheless, there is substantial collimation in these areas, which contrasts with the broad regions nearer to the optical galaxy.

Once at the outer hot spots of the components, the energy, whether carried by mechanism (a), (b) or (c), is deposited during an interaction with the static intergalactic medium. At this point various plasma processes take over, the energy is partitioned into a number of modes in ways which may differ for each of the three mechanisms (De Young, 1976), and radio emission commences. Thereafter the development is quite independent of the energy transport mechanism and the further one moves from the interaction front, the more similar the three models become. It is here, where we are concerned with the large scale structure of the components, that two major pieces of observational evidence emerge from the present work:

(1) The variation in spectral index between 21 and 49 cm is remarkably small, even over distances of many hundreds of kpc.

(2) There exist large scale magnetic fields that are well ordered over equally great lengths.

We shall begin by considering the spectral index variations, in particular those in the western lobe, 1549+20, for, being the larger of the two, it places the severest strain on any model. Because of inverse Compton losses on the universal microwave background in addition to synchrotron losses, the spectrum associated with the radiating material should steadily steepen as the material becomes older. Qualitatively we would then have the observed situation in which the bright outer heads, associated with the youngest relativistic material, have a flatter spectrum than the tail, and the spectrum along the tail becomes increasingly steeper as the distance to the outer hot spots increases. However a quantitative analysis shows that the true scenario cannot be quite so simple. Using the expressions for synchrotron emissivity given by Ginzburg and Syrovatskii (1964) and the equations for radiation losses given by van der Laan and Perola (1969) one can show that the observed spectral index, α, between frequencies ν_1 and ν_2 is related to the injection spectral index ν_0 by (see also Segalovitz, 1976)

$$\alpha \simeq \alpha_0 - \frac{\gamma_0 - 2}{\ln \frac{\nu_2}{\nu_1}} \ln \left\{ \frac{(1-\mu H_x^2 E_1 t)}{(1-\mu H_x^2 E_2 t)} \right\}, \qquad (2)$$

where ν_1 = lower frequency, in Hz, ν_2 = higher frequency, in Hz, $\gamma_0 = -2\,\alpha_0 + 1$, μ = a constant, which in cgs units is $1.57\ 10^{-3}$, t = time since particles were injected, in s, $H_x^2 = H^2 + H_c^2$, where H = equipartition magnetic field and $H_c = 4\ (1+z)^2\ 10^{-6}$ Gauss is the magnetic field equivalent of the universal microwave radiation density. We make the simplifying assumption that the only frequency at which an electron of energy E radiates is the frequency of maximum emission power, i.e.

$$E_1 \sim \left(\frac{\nu_1}{1.41\ 10^{18}\ H} \right)^{1/2} \quad \text{and} \quad E_2 \sim \left(\frac{\nu_2}{1.41\ 10^{18}\ H} \right)^{1/2},$$

where all units are cgs.

Assume that the injection spectral index, α_0, has the value -0.78 seen at the far western end at the hot spots. Then if there are no diffusion losses, the maximum time for the spectrum to decay to a spectral index of ~ -1.1 (that seen in the eastern part of 1549+20) is $\sim 2\ 10^7$ years according to Equation (2) above. Now, the 6 cm map of the component A and B region showed that the presumed injection site has a lateral width of only ~ 40 kpc whereas the "old" part of 1549+20, component D, where $\alpha \leqq -0.93$ (and thus older than $\sim 1.4\ 10^7$ years) has a lateral width of ~ 409 kpc. For material to expand from a region centred on the source major axis and having a radius of < 20 kpc to one with radius ~ 205 kpc in $\sim 1.4\ 10^7$ years requires an expansion velocity of $\sim 1.3\ 10^4$ km/s.

What is the likely expansion velocity? The "generalized sound speed" (Longair et al., 1973)—(internal energy/mass)$^{1/2}$—is applicable here. For magnetic fields as strong as the equipartition value this is equivalent to the Alfvén speed. As Table 6 shows, Alfvén speeds in the relatively compact features A and B as well as the broad region D are roughly an order of magnitude below that required by the simple lifetime estimate made above. This conflict implies that either,

(1) the equipartition magnetic field strength, and thus thermal electron densities derived assuming equipartition, are not valid, or

(2) the expansion rate is indeed less than $1.3\ 10^4$ km/s.

Considering the first possibility, what happens if we drop the equipartition assumption? One can increase the Alfvén speed, $H/(4\pi\rho)^{1/2}$, by increasing H and lowering ρ. It is possible to do this with the constraint that H and ρ are interrelated by the depolarization [Eq. (1)]. At the same time, of course, the time for the spectral index to decay from -0.78 to -1.1 decreases as the field strength increases [Eq. (2)]. One can iterate the solution until the Alfvén (or expansion) speed for component D and time for spectral decay attain convergence. Unfortunately, convergence is reached only when the expansion speed exceeds the speed of light. Rejecting this physically impossible situation, we consider what happens if we increase the sound speed. This can be done by lowering the magnetic field strength until the sound speed increases to $1.3\ 10^4$ km/s (the radiation lifetime does not change since inverse Compton losses dominate) keeping in mind the interrelationship between H and ρ (and hence component mass) and internal energy and H [Pacholczyk, 1970; Eq. (7.11)]. To increase the sound speed by a factor of 10 means changing H by 10^{-4} and

results in an increase of internal energy (above the equipartion value) of 10^6.

Apart from its unpalatable consequences with respect to total energy and magnetic field strength (resulting in a much increased inverse Compton emissivity) there is a more general problem, which also appears if we raise the sound speed by increasing the internal energy of the thermal (non-relativistic) plasma. This is the development of turbulence, which we discuss further below. As we note there, even if there is turbulence near the hot spots, the time scales are still sufficiently long that the large departures from equipartition required to keep the expansion speed high will probably have disappeared before component D attains its suggested age. Moreover, the very presence of turbulence would mean *in situ* acceleration anyway (see below), and the increased energy of the thermal gas will promote expansion, resulting in catastrophic adiabatic losses. Consequently, despite the steepening of the spectral index in this part of 1549+20 relative to the value of ~ -0.78 seen at the outer western head, there is almost certainly *in situ* acceleration in component D. (Note that the gap between the eastern end of component D and the nuclear source might be indicative of a region where acceleration has ceased and thus synchrotron emission is no longer visible.)

The conclusion that *in situ* acceleration is necessary is further bolstered by the fact that both 1549+20 and 1550+20 have simple power law spectra, without spectral steepening, to at least 2700 MHz (Section 4). Thus the relativistic electrons responsible for the radio emission must be younger than $\sim 2.4\ 10^7$ years or we would begin to see the spectral steepening expected from radiation losses (van der Laan and Perola, 1969). We argued above, however, that at least part of 1549+20, component D, was probably about $2.2\ 10^8$ years old. If 1550+20 has also expanded to its present size from an original size comparable to that of components A and B, it too must be $>10^8$ years old since its Alfvén velocity is ~ 590 km/s (Table 6). Thus *in situ* acceleration must be occurring during the lifetimes of the extended radio lobes.

The above analysis originated from the consideration that any change in spectral index was associated with aging and energy losses. Alternative explanations for the spectral index variations do exist. Assume that the relativistic electrons in the source have everywhere the same energy spectrum, but this spectrum has a spectral index which changes as a function of energy. The frequency of emission is given by $\nu \propto HE^2$, so that a change in the magnetic field strength would result in electrons of different energy radiating at the same frequency in different parts of the source depending upon the field strength. Then the spectral index between the two observed frequencies might well change. In 1549+20 the equipartition magnetic field strength decreases from $\sim 5\ \mu$G in components A and B to $\sim 1.7\ \mu$G in the eastern part. Now for electrons of the same energy, this implies that the frequency of radiation in A and B is a factor ~ 3 higher than in the outer lobes, or approximately, electrons radiating in the wavelength region from 21 to 6 cm in components A and B radiate in the 49 to 21 cm range in the eastern part of 1549+20. We saw earlier in Section 4b that the spectrum between 21 and 6 cm in components A and B was, if anything, flatter than the 21–49 cm spectrum in this region. Therefore if the electron energy spectrum was everywhere the same but had a bend which shifted through a particular wavelength interval because of variations in magnetic field strength, we would expect that the 21 to 49 cm spectrum in the eastern part should be similar or flatter than the "hot spot" spectrum. This effect is not seen. Note that this alternative does not eliminate the need for *in situ* acceleration.

None of the radio source models mentioned at the beginning of this section incorporates a mechanism for reaccelerating particles once they have left the region of the hot spot. However, Pacholczyk and Scott (1976) have considered acceleration by turbulence, and in particular its application to tailed radio galaxies. Superficially, 3C 326 would seem to be a good candidate for their model—for one thing, the degree of polarization (and hence magnetic field order) increases in 1549+20 as one progresses from the outer hot spots toward the central galaxy (Fig. 10). Note, however, that the drop in degree of polarization in the centre of component D is largely the result of vector cancellation between the northern and southern regions (Figs. 1c and 2c). This fact should not be ignored when considering the low degree of polarization which generally prevails in the region of the hot spots—as the 6 cm observations show, there is strongly polarized emission from at least one position (Fig. 3).

According to Pacholczyk and Scott's model, turbulence grows from instabilities which develop at the interface between the outward moving plasma and the motionless intergalactic medium. Turbulence in the plasma implies amplification of the magnetic field, which produces betatron acceleration of the relativistic particles. It also means that initially, the internal energy is dominated by the thermal plasma, but this energy is transferred to the magnetic field and relativistic particles until equipartition is achieved.

The first problem is that in the highly turbulent region near the hot spot, the degree of polarization should be very low, i.e. $\leqq 1\%$. For the radio tails this is the case, but it does not seem to be so for 3C 326. Even if we ignore the highly polarized region found at 6 cm (Fig. 3), it is clear that strong polarization emanates from between components A and B (Fig. 10). Even if strong turbulence does occur near A, the evidence suggests that it has ceased between A and B.

Furthermore, the time scale for field amplification estimated by Pacholczyk and Scott is very short for the

large galaxies. While relatively short fractional acceleration times are acceptable in the radio tails, where the distances are relatively small and where there is evidence for spectral steepening anyway, they appear insufficient for 3C 326. This implies, moreover, that large departures from energy equipartition quickly die out and that the Alfvén speed probably is a reasonable parameter for estimating rates of expansion in the more extended regions.

Pacholczyk and Scott do point out that in Phase II of their model, where strong turbulence has died out but some acceleration continues, the persistence of a degree of turbulence will not prevent the linear polarization from growing to moderately high values. Clearly more work is needed to determine how much energy can be extracted from such a process over much greater distances and in the presence of substantial expansion, a factor whose role is minor in this stage of radio tails. (We emphasize that none of the above should be interpreted as a criticism of Pacholczyk and Scott's model, which was explicitly developed for radio tails.)

Finally, we reiterate that 3C 326 strikingly underlines the need for *in situ* particle acceleration. Because of the great distances and time scales involved this must occur over much of the lifetime and throughout the entire source. The process must occur while the magnetic field retains a high degree of order in nearly all regions. Furthermore, the energy spectrum of particles produced must not vary greatly. Turbulence may well play a role, but mechanisms for developing or maintaining turbulence within the components may be required. Some sort of two component model—in which compact acceleration centres feed high energy particles into a smooth, large scale magnetic field—might be necessary.

Turning again to the interaction with an external medium—if we assume that the eastern part of 1549+20 has an age of $\sim 2.2\ 10^8$ years and that the relativistic material there was originally deposited by the particle accelerator presently associated with the outer hot spots the average velocity of the particle ejector is ~ 936 kpc/$2.2\ 10^8$ yr, or $\sim 4.1\ 10^3$ km s^{-1}. We can use this velocity to estimate the density of any intergalactic gas surrounding 1549+20 if we assume that it has had a retarding effect on the diffuse material in component D, preventing it from travelling along with the hot spots. For the intergalactic material to retard the emitted relativistic material $\rho_{ig} v^2 \sim 1/3\ U$ where ρ_{ig} = density of intergalactic medium, v = velocity at which the ejected relativistic material impinges on the external intergalactic medium and U = energy density inside the relativistic gas. From Table 4, use of the average conditions within 1549+20 yields $\rho_{ig} \sim 3\ 10^{-7}$ H atoms cm^{-3}. Thus only a very small intergalactic gas density is necessary to provide a retarding agent. Use of the average internal energy density may yield too low a value for the retarding density since lateral expansion has probably taken place as we discussed earlier. If we assume that the internal energy density of the relativistic gas at the time of initial interaction with the intergalactic medium is more likely $\sim 2.6\ 10^{-12}$ erg cm^{-3} (the equipartition conditions in the hot spots—Table 5) then the external density increases to $\sim 3\ 10^{-6}$ cm^{-3}.

If this gas were to exert any constraining influence on the region to the east of components A and B by thermal confinement then its temperature must be $T \sim \frac{4\,U}{9\,k\rho_{ig}}$. Thus $T \geqq \sim 2.2\ 10^8$ K. Such high temperatures might well be attained in an intracluster gas (e.g. Gull and Northover, 1975). However there is little evidence that 3C 326 lies within a cluster. The optical galaxy does lie just to the southwest of the Zwicky compact cluster 1550.1+2019 (Zwicky and Herzog, 1963) which would, however, be about twice as distant as 3C 326 according to Zwicky's estimate. Thus we think that the cluster is a background object unassociated with 3C 326. The low external density calculated above also provides some evidence that the radio galaxy lies outside a cluster. Some clusters, at least, must have gas densities of 10^{-3} to 10^{-4} atoms cm^{-3} if current theories to explain the shapes of the head-tail radio galaxies seen within clusters are valid (Jaffe, 1977; Wilson and Vallée, 1977). However the calculated values for the temperature, $2.2\ 10^8$ K, are quite consistent with those expected if the observed diffuse X-ray background originated from a hot intergalactic gas (Field, 1972).

We turn our attention to the eastern lobe, 1550+20, and note briefly that arguments similar to those discussed above regarding the spectral index and age suggest that there too *in situ* acceleration must occur. An interesting feature of this component is the large number of compact emission features seen in Figure 4 which (assuming their existence is confirmed in a map with better signal/noise) may offer an escape route from the well known adiabatic loss dilemma. These regions, having half power widths of only a few tens of kpc, would appear to emit a considerable fraction of the total flux (36%) from this lobe. If they partake of the general expansion of the component but themselves retain a constant volume, and thus a nearly constant magnetic field, the adiabatic loss problem may be alleviated. Another possibility is that they represent areas where the energy density is high because particle acceleration is occurring.

A striking feature of 3C 326 is the difference between the lengths of the two components. It is unlikely that this difference is the result of severe foreshortening in 1550+20, as in that case it is probable that 3C 326 would appear bent. Even if there is foreshortening, it probably does not seriously affect the calculated equipartition parameters: if the depth through 1550+20 were ~ 1000 kpc (about the projected length of 1549+20) the magnetic field strength, minimum energy density and thermal electron density would be approximately

$1.3\,10^{-6}$ Gauss, $1.6\,10^{-13}$ erg cm^{-3}, and $2.6\,10^{-5}$ cm^{-3}, respectively. These values are not very different from those listed in Tables 4 and 6.

Perhaps the most interesting result to emerge from the present observations is the existence of a magnetic field that is highly ordered and uniform over a scale of many hundreds of kpc (up to $\sim$550 kpc in the part of 1549+20 lying to the west of $RA = 15^h49^m27^s.5$). Since intrinsic degrees of polarization of up to 50% are found in the full resolution 21 cm observations, the random component of the field must be small. The existence of such a well ordered field obviously exerts a severe constraint on theories for the evolution of the outer components of radio sources. However a detailed discussion of this problem is beyond the scope of the present paper.

6. Conclusion

The main results from this work are the following:

(1) 3C 326 is a giant radio galaxy whose projected linear extent is $\sim$1.7 Mpc.

(2) The very small variation in the spectral index over distances of hundreds of kpc implies that local *in situ* acceleration must occur within the outer radio lobes, probably throughout the entire radio emitting region.

(3) While some of the acceleration may be due to plasma turbulence, this cannot occur throughout the entire radio source.

(4) Although there are compact emission features in the outer radio lobes, no single compact features contain a predominant amount of flux density.

(5) The source most likely does not lie within a cluster and the external gas density would appear to be very low, only $\sim 3\,10^{-6}$ atoms cm^{-3}.

(6) The projected magnetic field is oriented predominatly along the major axis of the radio source.

Acknowledgements. We thank the Westerbork telescope and reduction groups for their careful help in the data observation and reduction. Drs. E. M. Burbidge and H. Spinrad kindly communicated optical data in advance of publication. We are grateful to Prof. H. van der Laan for helpful discussions and to Dr. G. K. Miley, who was "the devil's advocate" on a number of occasions. Dr. G. Gisler also made helpful comments. P. den Hoed, J. Ober and L. Zuyderduin prepared the illustrations, and the manuscript was typed by J. Ekkelenkamp and W. Smit.

The Westerbork Radio Observatory is operated by the Netherlands Foundation for Radio Astronomy with the financial support of the Netherlands Organization for the Advancement of Pure Research (Z.W.O.).

References

Artyukh, V.S., Vitkevich, V.V., Dagkesamanskii, R.D., Kozhuklov, V.N.: 1969, *Soviet Astron. A. J.* **12**, 567
Baars, J.W.M., Hooghoudt, B.G.: 1974, *Astron. Astrophys.* **31**, 323
Baker, J.R.: 1974, *Mem. Soc. Astron. Ital.* **45**, 579
Blandford, R.D., Rees, M.J.: 1974, *Monthly Notices Roy. Astron. Soc.* **169**, 395
Bridle, A.H., Davis, M.M., Fomalont, E.B., Lequeux, J.: 1972, *Astron. J.* **77**, 405
Brouw, W.N.: 1971, Doctoral Thesis, Leiden University
Burn, B.J.: 1966, *Monthly Notices Roy. Astron. Soc.* **133**, 67
De Young, D.S.: 1976, *Ann. Rev. Astron. Astrophys.* **14**, 447
Dickel, J.R., Yang, K.S., McVittie, G.C.: 1967, *Astron. J.* **72**, 757
Field, G.B.: 1972, *Ann. Rev. Astron. Astrophys.* **10**, 227
Gardner, F.F., Whiteoak, J.B., Morris, D.: 1975, *Australian J. Phys. Astrophys. Suppl.* **35**, 1
Ginzberg, V.L., Syrovatskii, S.I.: 1964, *The Origin of Cosmic Rays*, Pergamon Press
Gull, S.F., Northover, K.J.E.: 1975, *Monthly Notices Roy. Astron. Soc.* **173**, 585
Harten, R.H.: 1975, Netherlands Foundation for Radio Astronomy—ITR 121
Högbom, J.A., Brouw, W.N.: 1974, *Astron. Astrophys.* **33**, 289
Höglund, B.: 1967, *Astrophys. J. Suppl.* **15**, 61
Holden, D.J.: 1969, *Monthly Notices Roy. Astron. Soc.* **145**, 67
Jaffe, W.J.: 1977, IAU *Symposium No. 74: Radio Astronomy and Cosmology*, Reidel, Holland (in press)
Kellerman, K.I., Pauliny-Toth, I.I.K., Williams, P.J.S.: 1969, *Astrophys. J.* **157**, 1
Longair, M.S., Ryle, M., Scheuer, P.A.G.: 1973, *Monthly Notices Roy. Astron. Soc.* **164**, 243
Mackay, C.D.: 1969, *Monthly Notices Roy. Astron. Soc.* **145**, 31
Pacholczyk, A.G.: 1970, *Radio Astrophysics*, W. H. Freeman and Co.
Pacholczyk, A.G., Scott, J.S.: 1976, *Astrophys. J.* **203**, 313
Readhead, A.C.S., Hewish, A.: 1974, *Mem. Roy. Astron. Soc.* **78**, 1
Segalovitz, A.: 1976, Doctoral Thesis, Leiden University
Shimmins, A.J., Day, G.A.: 1968, *Australian J. Phys.* **21**, 377
Smith, H.E., Spinrad, H., Smith, E.O.: 1976, *Publ. Astron. Soc. Pacific* **88**, 621
Smith, M.A.: 1968, Doctoral Thesis, Cambridge University
Spoelstra, T.A.Th.: 1972, *Astron. Astrophys.* **21**, 61
Vallée, J.P., Kronberg, P.P.: 1975, *Astron. Astrophys.* **43**, 233
Van der Laan, H., Perola, G.C.: 1969, *Astron. Astrophys.* **3**, 468
Van Someren Gréve, H.W.: 1974, *Astron. Astrophys. Suppl.* **15**, 343
Véron, M.P., Véron, P., Witzel, A.: 1974, *Astron. Astrophys. Suppl.* **13**, 1
Viner, M.R., Erickson, W.C.: 1975, *Astron. J.* **80**, 931
Weiler, K.W.: 1973, *Astron. Astrophys.* **26**, 403
Willis, A.G., Strom, R.G., Wilson, A.S.: 1974, *Nature* **250**, 625
Wilson, A.S., Vallée, J.P.: 1977, *Astron. Astrophys.* (to be published)
Wilson, A.S., Weiler, K.W.: 1976, *Astron. Astrophys.* **49**, 357
Zwicky, F., Herzog, E.: 1963, *Catalogue of Galaxies and of Clusters of Galaxies*, Vol. II, California Institute of Technology